PHYSICAL REVIEW B **110**, 115202 (2024)

Giant thermoelectric effect governed by unique two-dimensional electronic structure and strong anharmonicity in layered nitrides

Mengli Yao, Min Li, Long Zhang [*] and Hui Wang [†]
School of Physics, Hunan Key Laboratory of Super Microstructure and Ultrafast Process,
Hunan Key Laboratory of Nanophotonics and Devices, State Key Laboratory of Powder Metallurgy,
Central South University, Changsha 410083, China

(Received 25 July 2024; revised 26 August 2024; accepted 29 August 2024; published 11 September 2024)

Layered complex nitrides have emerged as a novel class of thermoelectric materials due to their unique geometrical and electronic structures. In this work, we employ density functional theory calculations combined with Boltzmann transport equation and thermal transport unified theory to explore the electrical and thermal transport properties and thermoelectric performance of layered nitrides AMN_2 (A = Sr, Ba; M = Ti, Zr, Hf). It is found that the AMN_2 family exhibits a large Seebeck coefficient and high power factor, ascribed to its multiband degeneracy and the presence of unique two-dimensional (2D) electronic structure. As the atomic mass of M increases, the lattice thermal conductivity κ_L decreases significantly. In particular, $BaHfN_2$ demonstrates ultralow lattice thermal conductivity of 0.18 W/mK at room temperature. Even after accounting for both the particlelike propagation and wavelike phonon tunneling transport, ultralow κ_L is found across a wide temperature range. The ultralow κ_L is mainly attributed to the strong anharmonicity in $BaHfN_2$ as reflected by the high phonon-phonon scattering rate and short phonon lifetime. Importantly, we find that p-type $BaHfN_2$ exhibits a high figure of merit (ZT), achieving values of 2.19 at 300 K and 7.29 at 900 K, respectively. Additionally, through strain engineering, applying a moderate tensile stress of 0.5% remarkably increases the ZT of p-type increases to 2.58 at 300 K and reaches a maximum of 9.02 at 900 K, respectively. The present work unveils the importance of unique 2D electronic structures and strong anharmonicity induced by the weak-bonded heavy element on the thermoelectric performance, suggesting that the layered AMN_2 family is a promising candidate for the development of high-performance thermoelectric devices.

DOI: 10.1103/PhysRevB.110.115202

I. INTRODUCTION

Thermoelectric (TE) devices convert waste heat into electrical energy from the temperature gradient, and vice versa from the electrical gradient. The efficiency of the thermoelectric device is governed by the performance of TE materials [1–3], as evaluated by a dimensionless figure of merit, $ZT = S^2\,\sigma T/(\kappa_L + \kappa_e)$, where S, σ, T, κ_L, and κ_e are the Seebeck coefficient, electrical conductivity, absolute temperature, lattice thermal conductivity, and electron thermal conductivity [4,5], respectively. Clearly, a higher TE performance can be achieved by increasing the power factor ($\mathrm{PF} = S^2\sigma$) or suppressing the thermal conductivity [6,7]. However, the bottleneck in optimizing ZT is the complex and interdependent relationship between intrinsic parameters such as S, σ, and κ [8].

To improve the TE conversion efficiency, tremendous efforts have been made in the past few years [9–12]. On the one hand, the PF is enhanced by band structure engineering which was demonstrated as an effective method to regulate the electrical transport properties of materials [13,14]. Tuning the relative positions of light and heavy bands near the Fermi level in PbTe [15] and KAgSe [16], along with maximizing the valley degeneracy of these bands, can effectively improve the Seebeck coefficient and overall thermoelectric performance of these materials. On the other hand, the lattice thermal conductivity is suppressed through the enhancement of phonon scattering rate and anharmonicity of the materials [17,18]. Introduction of dense dislocations in PbSe through Te/S alloying and Cu interstitial doping could induce strong phonon scattering, resulting in an ultralow lattice thermal conductivity [19]. Yang *et al.* reported that rough silicon nanowires demonstrate Seebeck coefficient and electrical resistivity values comparable to doped bulk Si, yet possess significantly lower thermal conductivity [20]. Additionally, two-dimensional PtX_2 monolayer exhibits extremely low lattice thermal conductivity, ranging 0.207–0.643 $\mathrm{W\,m^{-1}\,K^{-1}}$, with the highest ZT of 1.65 at 300 K [21].

Recently, layered oxides were identified as promising thermoelectric [22,23] attributed to their unique two dimensional (2D) electronic structure embedded in the bulk crystal structure [24,25]. The most representative example is the 2D electron gas (2DEG) in the heterogeneous interface of $SrTiO_3$. For example, the degeneracy of cubic $SrTiO_3$ is disrupted at the $LaAlO_3/SrTiO_3$ interface [26,27], leading to the formation of Ti $3d_{xy}$ orbital dominated conduction band minimum (CBM) channel in the 2DEG layer. As a result, the material exhibits enhanced electron mobility and improved electrical conductivity. Alternatively, the insulating oxide layer composed of $(Bi_2O_2)^{2+}$ with ionic bonds serves as a charge reservoir in the thermoelectric BiCuSeO material,

---

[*] Contact author: L.zhang@csu.edu.cn

[†] Contact author: huiwang@csu.edu.cn

while the conductive selenide $(Cu_2Se_2)^{2-}$ layer with covalent bonds acts as the pathway for carrier transport, and substituting the Bi^{3+} with Sr^{2+} in BiCuSeO significantly enhances its electrical conductivity [28]. Layered complex nitrides of the $KCoO_2$ type exhibit strong anisotropy of the energy band and the large effective mass [23,29], showing better electrical transport properties than those of α-$NaFeO_2$ type and well-known TE material (e.g., $SrTiO_3$) [25]. However, the lattice thermal conductivity and overall thermoelectric performance of layered complex nitrides remain to be explored.

In this work, we systematically investigate the electrical and thermal transport properties along with thermoelectric performance of layered complex nitrides AMN_2 (A = Sr, Ba; M = Ti, Zr, Hf) through density functional theory (DFT), Boltzmann transport theory, and thermal transport unified theory. We find that the AMN_2 family exhibits high electrical transport properties due to the unique quasi-two-dimensional electronic structure. The cylindrical Fermi surface formed by the M-N atomic layer results in highly anisotropic and multidegenerate band structure that enhances the Seebeck coefficient and electrical conductivity. In particular, $BaHfN_2$ exhibits a high power factor and ultralow lattice thermal conductivity attributed to strong anharmonicity. Therefore, an ultrahigh ZT of 2.19 at 300 K and 7.29 at 900 K are identified. Furthermore, strain engineering is able to improve its overall thermoelectric performance, reaching a maximum ZT value of 2.58 at room temperature under tensile strain of 0.5%. After considering the mechanism of wavelike phonons tunneling in $BaHfN_2$, we find that the wavelike contribution to the total thermal conductivity is as high as 51% and 67% at 300 and 900 K, respectively. Nevertheless, the lattice thermal conductivity of $BaHfN_2$ still remains rather small, as low as 0.36 W/mK at room temperature; high ZT values remain across a wide temperature range.

II. COMPUTATIONAL DETAILS

We performed first-principles calculations [30] based on the density functional theory (DFT) as implemented in the Vienna *ab initio* simulation package (VASP) [31–33]. The electronic exchange correlation was modeled using the Perdew-Burke-Ernzerhof (PBE) functional within the generalized gradient approximation (GGA) [34–36]. The lattice structure and atomic positions were fully relaxed until the forces on each atom of structure were below 0.001 eV/Å, and the energy convergence criterion was set to 1×10^{-8} eV. The energy cutoff of the plane wave was 450 eV, and a Monkhorst-Park $12\times12\times6$ k-point grid in the Brillouin zone was used for static calculations. The phonon spectrum can be obtained by the PHONOPY code with the finite displacement method [37]. By introducing the second-order harmonic interatomic force constant (IFC) and third-order nonharmonic IFC, the phonon transport equation was solved using the SHENGBTE code [38], and the thermal transport properties of different materials were analyzed [39]. The Born effective charge and dielectric constant were calculated based on the density functional perturbation theory. After convergence testing, a $3\times3\times2$ supercell with atoms interaction cutoff reaching up to the sixth nearest neighbors was used (see Supplemental Material Fig. S1 [40]), and a $10\times10\times10$ q grid was considered to obtain more accurate lattice thermal conductivity.

The relaxation time was calculated by using the electron-phonon Wannier (EPW) module of QUANTUM ESPRESSO (QE) [41]. The energy cutoff values for the plane wave function and charge density were set to 70 and 280 Ry, respectively, and the energy convergence standard was set to 10^{-8} eV. The relaxation time was calculated using the Wannier interpolation method with $32\times32\times16$ q and k mesh. The electrical transport properties of materials, such as Seebeck coefficient, electronic conductivity, electronic thermal conductivity, power factor, and thermoelectric merit, are all calculated using the BOLTZTRAP code.

When the system under consideration reaches thermodynamic equilibrium, the phonon distribution satisfies the Bose-Einstein distribution $f_0(\omega)$. Then the Boltzmann transport equation can be written

$$\frac{\partial f_\lambda}{\partial t}_{\text{diffusion}} + \frac{\partial f_\lambda}{\partial t}_{\text{scattering}} = 0, \tag{1}$$

where λ is the index of phonon mode. Therefore

$$\frac{\partial f_\lambda}{\partial t}_{\text{diffusion}} = -\nabla T \cdot \boldsymbol{v}_\lambda \frac{\partial f_\lambda}{\partial T}. \tag{2}$$

The scattering term depends on the specific scattering process of phonons, when only two and three phonon processes are considered:

$$\boldsymbol{F}_\lambda = \tau_\lambda^0(\boldsymbol{v}_\lambda + \Delta_\lambda), \tag{3}$$

$$\frac{1}{\tau_\lambda^0} = \frac{1}{N}\left(\sum_{\lambda'\lambda''}^{+}\Gamma_{\lambda\lambda'\lambda''}^{+} + \sum_{\lambda'\lambda''}^{-}\frac{1}{2}\Gamma_{\lambda\lambda'\lambda''}^{-} + \sum_{\lambda'}\Gamma_{\lambda\lambda'}\right), \tag{4}$$

where $\boldsymbol{v}_\lambda$ is the group velocity of the phonon mode λ. Δ_λ measures the deviation from the relaxation time approximation (RTA), where $\Gamma_{\lambda\lambda'\lambda''}^{+}$, $\Gamma_{\lambda\lambda'\lambda''}^{-}$, and $\Gamma_{\lambda\lambda'}$ correspond to the scattering rates from three-phonon absorption and emission processes and isotopic effect, respectively. Once $\boldsymbol{F}_\lambda$ is evaluated by iteration, the thermal conductivity can be calculated as [38]

$$k_l^{\alpha\beta} = \frac{1}{k_B T^2 N\Omega}\sum f_0(f_0+1)(\hbar\omega_\lambda)^2 v_\lambda^\alpha v_\lambda^\beta \tau_\lambda, \tag{5}$$

where α and β represent the Cartesian axes, and Ω, N, and f_0 are the volume of the unit cell, the number of k points, and Bose-Einstein statistics, respectively. Further, ω_λ denotes the angular frequency of the phonon mode, v_λ^α and v_λ^β are the group velocity components, τ_λ is the self-consistent phonon lifetime, and k_B is the Boltzmann constant.

Using semiclassical Boltzmann transport theory, we calculated the thermoelectric transport properties of AMN_2 material. The Seebeck coefficient ($S_{\alpha\beta}$), electrical conductivity ($\sigma_{\alpha\beta}/\tau$), and electronic thermal conductivity ($\kappa_e^{\alpha\beta}/\tau$) are given as follows [42]:

$$S_{\alpha\beta}(T,\varepsilon_F) = \frac{1}{eT}\frac{\int v_\alpha(i,\boldsymbol{k})v_\beta(i,\boldsymbol{k})(\varepsilon-\varepsilon_F)\left[\frac{-\partial f_{\varepsilon_F}(T,\varepsilon)}{\partial\varepsilon}\right]d\varepsilon}{\int v_\alpha(i,\boldsymbol{k})v_\beta(i,\boldsymbol{k})\left[\frac{-\partial f_{\varepsilon_F}(T,\varepsilon)}{\partial\varepsilon}\right]d}, \tag{6}$$

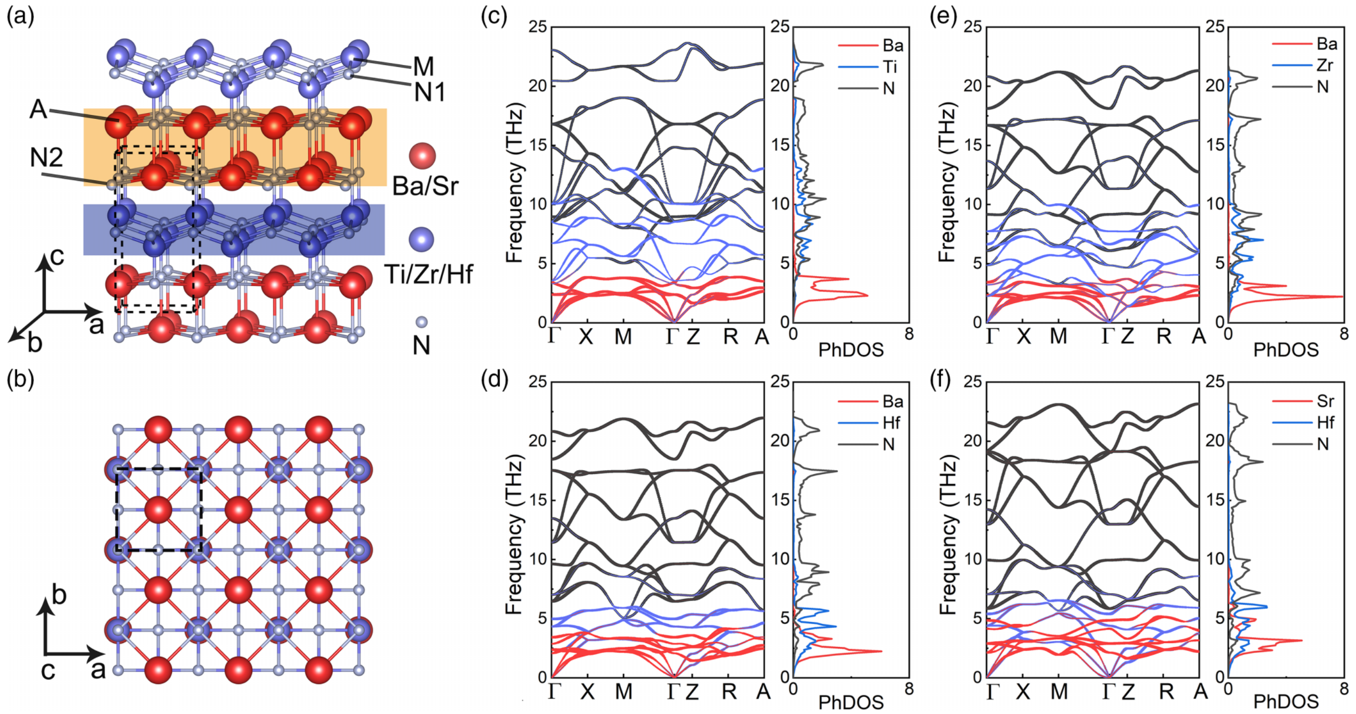

FIG. 1. Panels (a) and (b) show the top and side views of AMN_2 (A = Sr, Ba, and M = Ti, Zr, Hf), respectively. The structural units are shown by the black dashed line. Orange and blue boxes represent the insulation layer and transition metal layer. (c)–(f) Projected phonon dispersion spectra and projected density of states for four materials. Red, blue, and gray represent Ba/Sr atoms, Ti/Zr/Hf atoms, and N atoms, respectively.

$$\frac{\sigma_{\alpha\beta}(T,\ \varepsilon_F)}{\tau} = \frac{1}{\Omega}\int e^2 v_\alpha(i,\ \boldsymbol{k}) v_\beta(i,\ \boldsymbol{k})\left[\frac{-\partial f_{\varepsilon_F}(T,\ \varepsilon)}{\partial \varepsilon}\right] d\varepsilon, \tag{7}$$

$$\frac{\kappa_e^{\alpha\beta}(T, \varepsilon_F)}{\tau} = \frac{1}{e^2 T\Omega}\int e^2 v_\alpha(i, \boldsymbol{k}) v_\beta(i, \boldsymbol{k})(\varepsilon - \varepsilon_F)^2 \times \left[\frac{-\partial f_{\varepsilon_F}(T, \varepsilon_F)}{\partial \varepsilon}\right] d_\varepsilon, \tag{8}$$

where e and T are the electron charge and temperature, ε is the reduced energy, v is the group velocity along the studied direction, and τ is the relaxation time calculated by the electron-phonon Wannier method.

III. ELECTRICAL PROPERTIES

A. Crystal structure

The structures of layered nitrides AMN_2 (A = Sr, Ba; M = Ti, Zr, Hf) adopt the $KCoO_2$ type native superlattice [43]. The AMN_2 contains two different layers, namely, the M-N layer and the A-N layer, as shown in Figs. 1(a) and 1(b). The M cations are coordinated with five N atoms, resulting in four M-N(N1) bonds and one M-N(N2) bond, thereby forming the M-N carrier transport layer, while the A atoms are similarly coordinated with five N atoms in a square-base pyramidal geometry, creating the A-N insulation layer [44]. The optimized lattice parameters of $BaTiN_2$, $BaZrN_2$, $BaHfN_2$, and $SrTiN_2$, which closely match previously reported values [29], are listed in Table I.

B. Stability

To evaluate the stability, we first calculated the formation enthalpies [45] for $BaTiN_2$ (−5.19 eV), $BaZrN_2$ (−5.12 eV), $BaHfN_2$ (−5.60 eV), and $SrTiN_2$ (−5.86 eV). The negative formation enthalpies indicate that these materials are thermodynamically stable. We further employ *ab initio* molecular dynamics (AIMD) simulations under the canonical ensemble (*NVT*) to explore the thermal stability of the layered nitrides, as displayed in Supplemental Material Fig. S2 [40]. Using $BaHfN_2$ as a case study, we find that after simulating for 5000 fs at various temperatures, the structure of the material remains intact with no significant deformation observed. Additionally, both the total energy and temperature only slightly fluctuate around the equilibrium state in Figs. S2(d)–S2(f), indicating that $BaHfN_2$ exhibits excellent thermal stability at medium to high temperatures. It is worthwhile to note that $BaZrN_2$ and $BaHfN_2$ have been synthesized experimentally [46,47]. We then evaluate the dynamic stability of the AMN_2

TABLE I. Lattice constant a and c (Å), band gap E_g (eV), effective mass of electrons and holes [m_h and m_e (m_0)] in different directions, and relaxation time τ (fs) for $BaTiN_2$, $BaZrN_2$, $BaHfN_2$, and $SrHfN_2$.

Configurations	a	c	E_g	$m_h{}^x$	$m_h{}^z$	$m_e{}^x$	$m_e{}^z$	τ
$BaTiN_2$	4.02	8.11	0.62	−0.56	−1.90	0.20	78.11	1.74
$BaZrN_2$	4.20	8.49	1.00	−0.37	−7.80	0.21	35.03	9.72
$BaHfN_2$	4.15	8.48	1.25	−0.38	−4.37	0.21	32.77	9.30
$SrHfN_2$	4.04	8.28	1.54	−0.44	−4.27	0.23	38.83	25.98

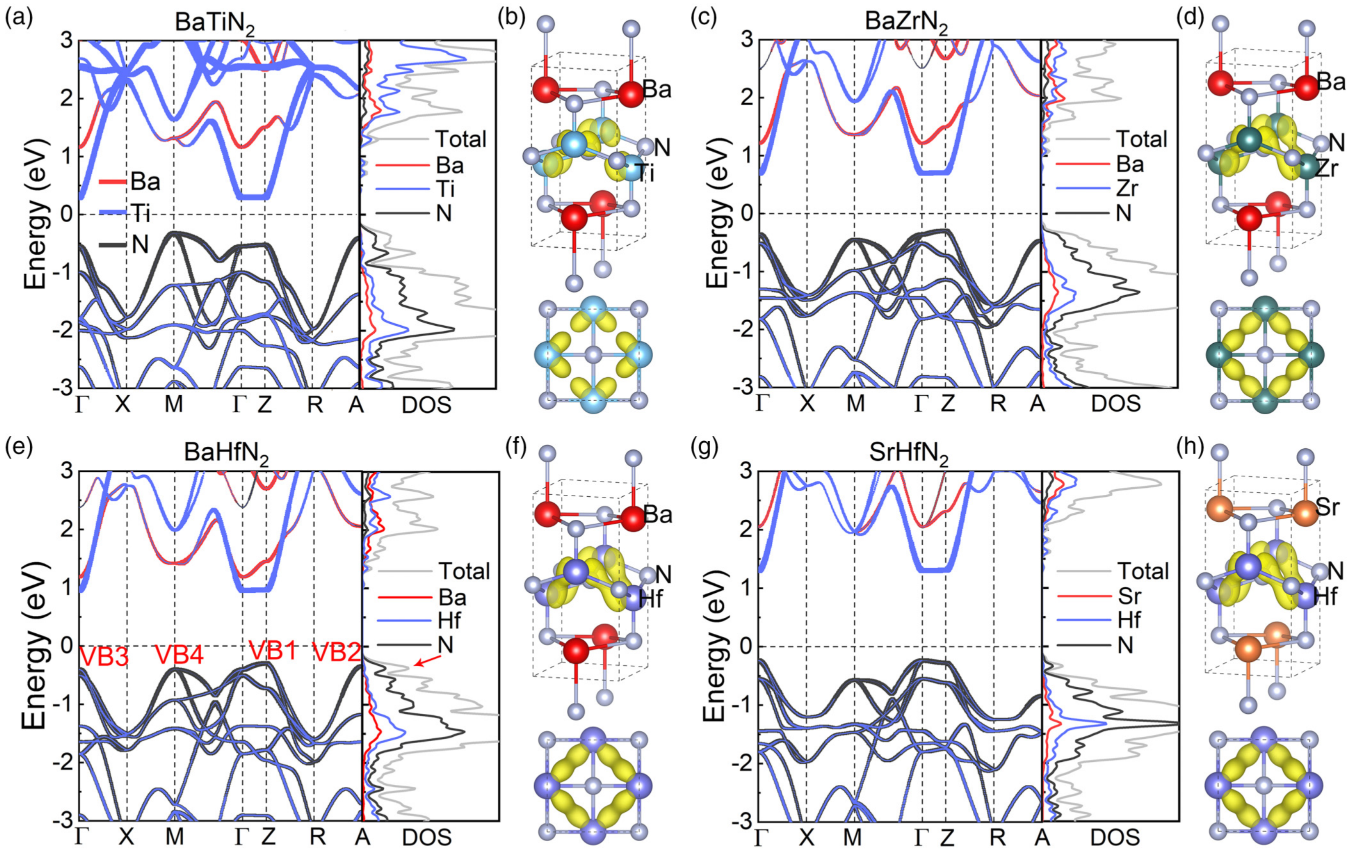

FIG. 2. Projected electronic band structure and projected density of states, and side view and top view of charge density of maximum conduction band in (a), (b) BaTiN$_2$, (c), (d) BaZrN$_2$, (e), (f) BaHfN$_2$, and (g), (h) SrHfN$_2$. Red, cyan, green, blue, orange, and gray represent transition metal atoms Ba, Ti, Zr, Hf, Sr, and N, respectively. Γ, *X*, *M*, *Z*, *R*, and *A* correspond to the first Brillouin zone internal coordinates (0, 0, 0), (0, 0.5, 0), (0.5, 0.5, 0), (0, 0, 0.5), (0, 0.5, 0.5), and (0.5, 0.5, 0.5), respectively.

through analysis of phonon spectra, as displayed in Figs. 1(c)–1(f). There is no imaginary frequency in the phonon spectrum in all the investigated materials.

C. Electronic properties

In BaMN$_2$ (M = Ti, Zr, and Hf), as the mass of transition metal *M* atoms increases, the entire phonon spectrum frequency gradually shifts downwards in frequency. Additionally, the hybrid contribution of *M* and *N* atoms transitions from dominating the high-frequency to the low-frequency range. This trend is supported by the projected phonon density of states (PhDOS) distribution, where the contribution of Ti, Zr, and Hf atoms shifts towards low frequencies. Compared with BaHfN$_2$, the phonon spectrum of SrHfN$_2$ exhibits the opposite trend, particularly with a stiffening of the low-frequency modes. These shifts in the phonon spectrum, especially the changes of phonon band in the low-frequency range, have significant impact on the thermal transport properties.

We then explored the electronic band structure and projected density of states (DOS) of the AMN$_2$, as shown in Fig. 2. Notably, the minimum conduction band (CBM) is mainly contributed by *A* and *M* atoms, while the maximum valence band (VBM) is mainly contributed by N atoms. The results show that, except for SrHfN$_2$, the other three materials have an indirect band gap with the CBM located at the Γ point; the Brillouin zone is shown in Supplemental Material Fig. S3. For BaMN$_2$ (M = Ti, Zr, and Hf), as the mass of *M* element increases, the VBM shifts from the *M* point to the *Z* point, while the CBM continues to rise at the Γ point, resulting in a gradual increment of band gap from 0.62, 1.00, to 1.25 eV. While the VBM shifts to the Γ point in SrHfN$_2$, resulting in a larger band gap of 1.54 eV. It is clear that the CBM exhibits significant dispersion in the in-plane direction, indicating that electrons move with a smaller effective mass within the plane. However, along the vertical direction (i.e., Γ-*Z*), the CBM appears almost flat, suggesting localization of electrons in this direction. The VBM displays dispersion along the Γ-*X* and Γ-*M* directions, but shows weak dispersion in the direction of Γ-*Z*. It is worthwhile to note that orbital degeneracy and obvious multivalley degeneracy appear in the valence band (VB) of BaHfN$_2$, as displayed in Fig. 2(e). Within the plane, the energy values of VB1 and VB2 differ by only 0.06 eV, while VB3 and VB4 exhibit nearly identical values. This convergence of multiple valence bands results in a pronounced total density of states near the VBM as indicated by the red arrow in the corresponding DOS diagram, which is conducive to the generation of a large Seebeck coefficient.

Interestingly, we observe that the CBM is mainly contributed by *A*-*d* and *M*-*d* orbitals, while the VBM is mainly contributed by N-*p* orbitals as in Fig. 3. The electron density distribution of CBM reveals that electrons are directed

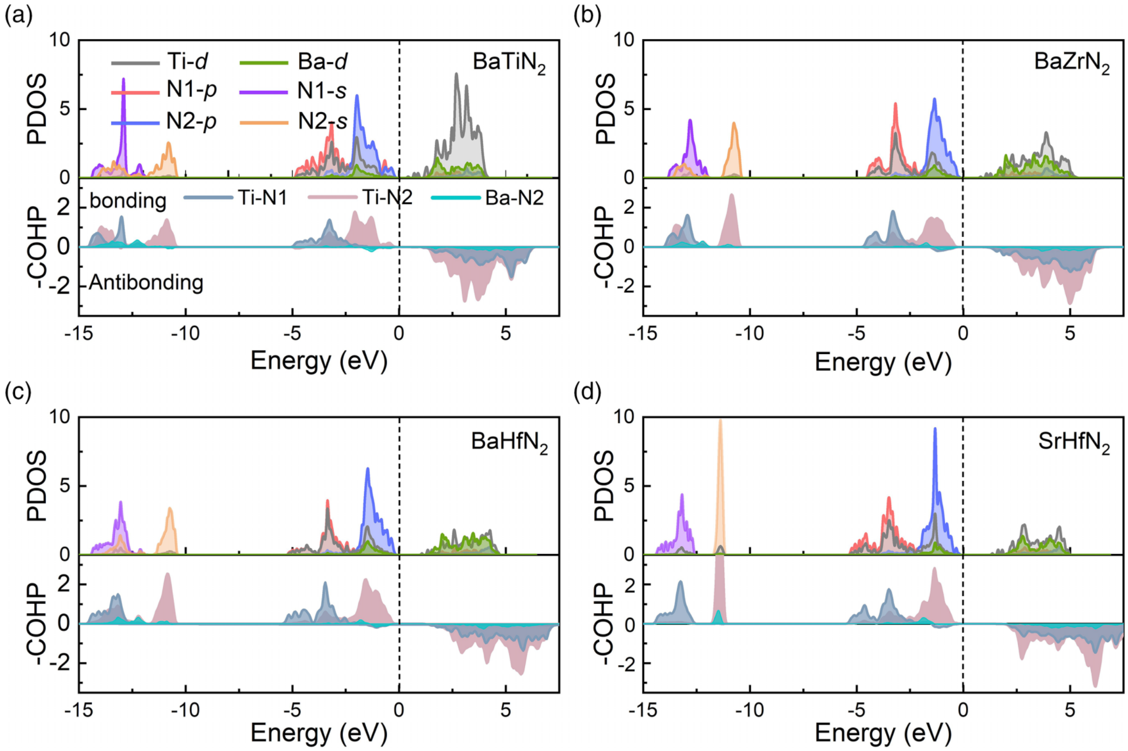

FIG. 3. (a)–(d) Calculated orbital projected orbital density of states (PDOS) and the −COHPs for *M*-N1, *M*-N2, and *A*-N2 bonds of BaTiN$_2$, BaZrN$_2$, BaHfN$_2$, and SrTiN$_2$. The Fermi energy level is set to 0 eV.

towards the nearest transition metal *M* atom and confined within the *M*-N1 layer in Figs. 2(b), 2(d), 2(f), and 2(h). As the atom mass of the *M* increases, the charge density gradually rises, leading to an increment in electron density. The increment in electron density within the *M*-N1 layer is beneficial for the electrical transport properties. This suggests that the *AM*N$_2$ family has highly anisotropically electrical transport properties in the z and x/y direction, akin to those characteristics of a 2D electron gas system [23]. The enhanced electrical transport properties are reflected by the calculated effective masses of electrons (m_e) and holes (m_h), as listed in Table I. It is clear that the electron effective masses of the *AM*N$_2$ family in the z direction is at least two orders of magnitude larger than that in the x direction. Similarly, compared to the x direction, the energy band arrangement of holes is smoother in the z direction, resulting in a larger hole effective mass (m_h^z) in the z direction than that in the x direction.

Then, we perform chemical bond analysis on *AM*N$_2$ based on the crystal orbital Hamilton population (COHP). The −COHP of the chemical bonds of *M*-N1, *M*-N2, and *A*-N2 is shown in Fig. 3. The −ICOHP value obtained by integrating −COHP into the Fermi energy level to estimate the binding strength of each bond is listed in Table II. By comparison, it can be seen that the bonding states of *M*-N1 and *A*-N2 are relatively weak. For example, the −ICOHP of Ti-N1 and Ba-N2 in BaTiN$_2$ are 2.89 and 0.40, respectively, which are significantly smaller than that of Ti-N2 (6.27), indicating strong bonding between *M* and N2. Similar bonding results have also been observed in other materials. In BaMN$_2$, the number of bonding states of Hf-N2(6.11) is less than that of Ti-N2(6.27) and Zr-N2(6.15), indicating the weakened interaction between heavy Hf and N2. It can also be observed from the projected orbital density of states that the overlap between the *d* orbitals of *M* atoms and the *p* orbitals of N2 atoms decreases with increasing the mass of *M* atoms, thus confirming the bonding strength of *M*-N2 follows the trend of Ti-N2 > Zr-N2 > Hf-N2. The mean square displacement (MSD) calculated by molecular dynamics simulations [48] indicates that atoms vibrate locally in their equilibrium positions in BaHfN$_2$. The atomic displacement parameter (ADP) suggests that a larger ADP indicates a relatively small binding of Ba atoms within the lattice, with weak bond cooperation between Ba atoms and their nearest neighbor N atoms (Supplemental Material Fig. S4), ultimately enhancing the anharmonicity and phonon scattering that give rise to ultralow thermal conductivity.

TABLE II. The −ICOHP values of different bond lengths in the *AM*N$_2$ structure; unit (eV).

Bond type	BaTiN$_2$	BaZrN$_2$	BaHfN$_2$	SrHfN$_2$
M-N1	2.89	3.17	3.31	3.58
M-N2	6.27	6.15	6.11	6.09
A-N2	0.40	0.42	0.44	0.52

IV. THERMOELECTRIC PROPERTIES

A. Thermal transport properties

To explore the thermal transport properties of *AM*N$_2$ family, we calculated the lattice thermal conductivity as displayed in Fig. 4(a). Clearly, we observe that the lattice thermal conductivity in BaMN$_2$ decreases as the atomic mass of *M*

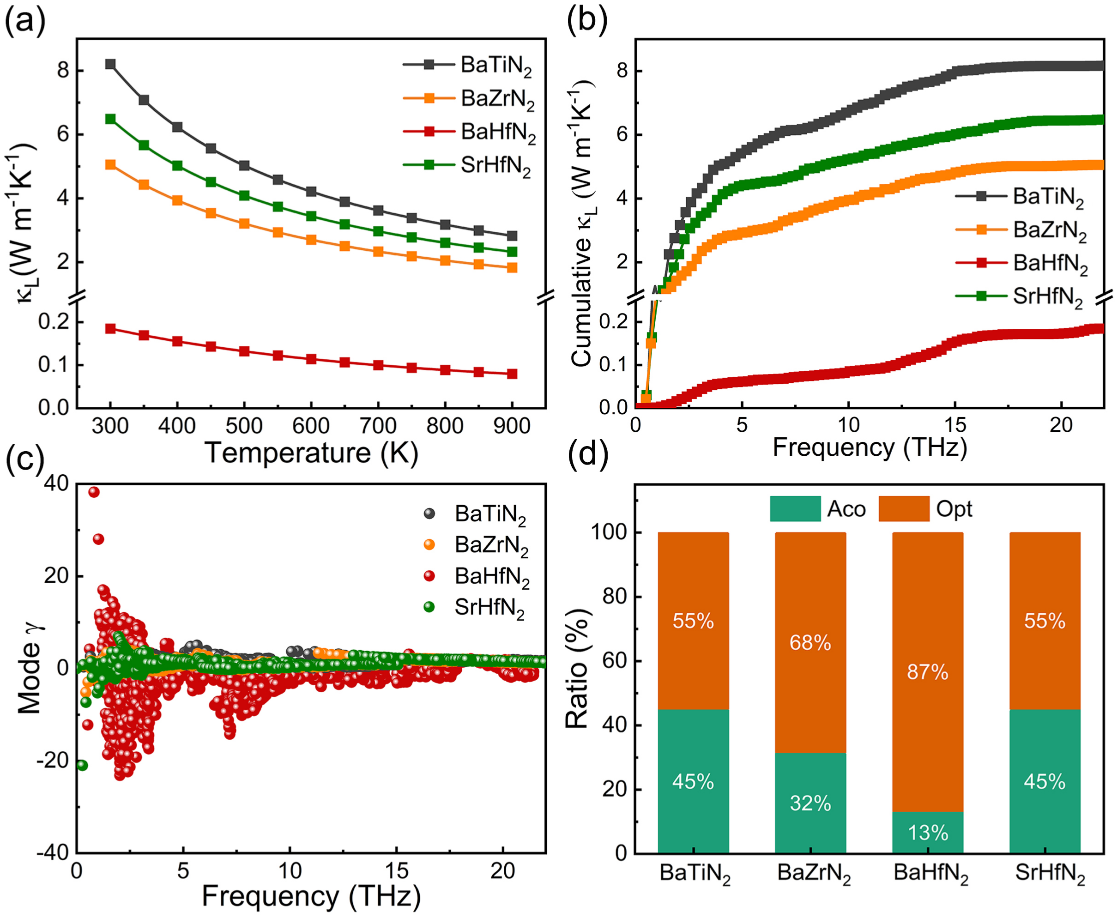

FIG. 4. (a) The temperature dependent lattice thermal conductivity κ_L and (b) frequency dependent cumulative thermal conductivity, (c) The Grüneisen parameter and (d) the percentage of optical and acoustic branches in thermal conductivity in AMN_2 structures.

increases. Particularly, $BaHfN_2$ exhibits an ultralow thermal conductivity with a value of 0.18 W/mK at 300 K, while replacing Ba with Sr leads to one order of magnitude increment in lattice thermal conductivity, with a value up to 6.49 W/mK at 300 K. The thermal conductivity accumulation shows that the overall thermal conductivity of AMN_2 is influenced by phonon scattering across both low and high frequencies, as displayed in Fig. 4(b). To evaluate the probability of three phonon scattering, we calculated the scattering phase space W, which includes both the adsorption (W^+) and emission (W^-) process, as shown in Supplemental Material Fig. S5. The relatively small differences of W^+ and W^- suggest that the number of available phonon scattering processes is insufficient to explain the source of ultralow κ_L in $BaHfN_2$. Instead, this phenomenon can be rationalized by the distribution of Grüneisen parameters, as shown in Fig. 4(c). At room temperature, the average range of Grüneisen parameters for $BaTiN_2$, $BaZrN_2$, and $SrHfN_2$ are quite close, ranging 1.51–1.86, 1.32–1.99, and 1.33–2.14, respectively. In contrast, $BaHfN_2$ has a significantly higher average value of 4.49, with a distribution range 2.95–20.34, indicating the strong anharmonicity in $BaHfN_2$. We then examined the contribution of acoustic and optical branches to κ_L at room temperature, as shown in Fig. 4(d). As the atomic mass of M increases, the contribution of the total optical branches to the thermal conductivity rises significantly, from 55% in $BaTiN_2$ to 87% in $BaHfN_2$. Since the lattice thermal conductivity is mainly dominated by the low-frequency acoustic phonons, the prominently increasing contribution of optical branches in AMN_2 greatly reduces their thermal conductivity. Compared to the $BaHfN_2$, the contribution of the optical branch decreases down to 55% in $SrHfN_2$, increasing remarkably the lattice thermal conductivity.

This can be further supported by the distribution of the phonon group velocity and phonon lifetime of the AMN_2 family, as shown in Figs. 5(a)–5(c) and Supplemental Material Fig. S6. We observe that the phonon group velocity is mainly related to the optical branch, and the phonon group velocity of $BaHfN_2$ (0.82 km/s) is a little bit smaller than that of $BaTiN_2$ (1.06 km/s), $BaZrN_2$ (0.93 km/s), and $SrHfN_2$ (0.88 km/s). Importantly, we observe that the phonon lifetime in $BaHfN_2$ decreases by two orders of magnitude compared to the other materials as shown in Figs. 5(d)–5(f). A shorter phonon lifetime indicates a stronger scattering process, resulting in a lower lattice thermal conductivity. For comparison, the phonon lifetime in $SrHfN_2$ is much longer, consistent with its high lattice thermal conductivity. It is worthwhile to note that the electronic thermal conductivity, particularly under p-type doping, is generally three orders of magnitude smaller than the lattice thermal conductivity as shown in Supplemental Material Fig. S7. Specifically, for $BaHfN_2$, the electronic thermal conductivity at the p-type doping concentration with the highest ZT value at 300 K is 0.006 W m^{-1} K^{-1},

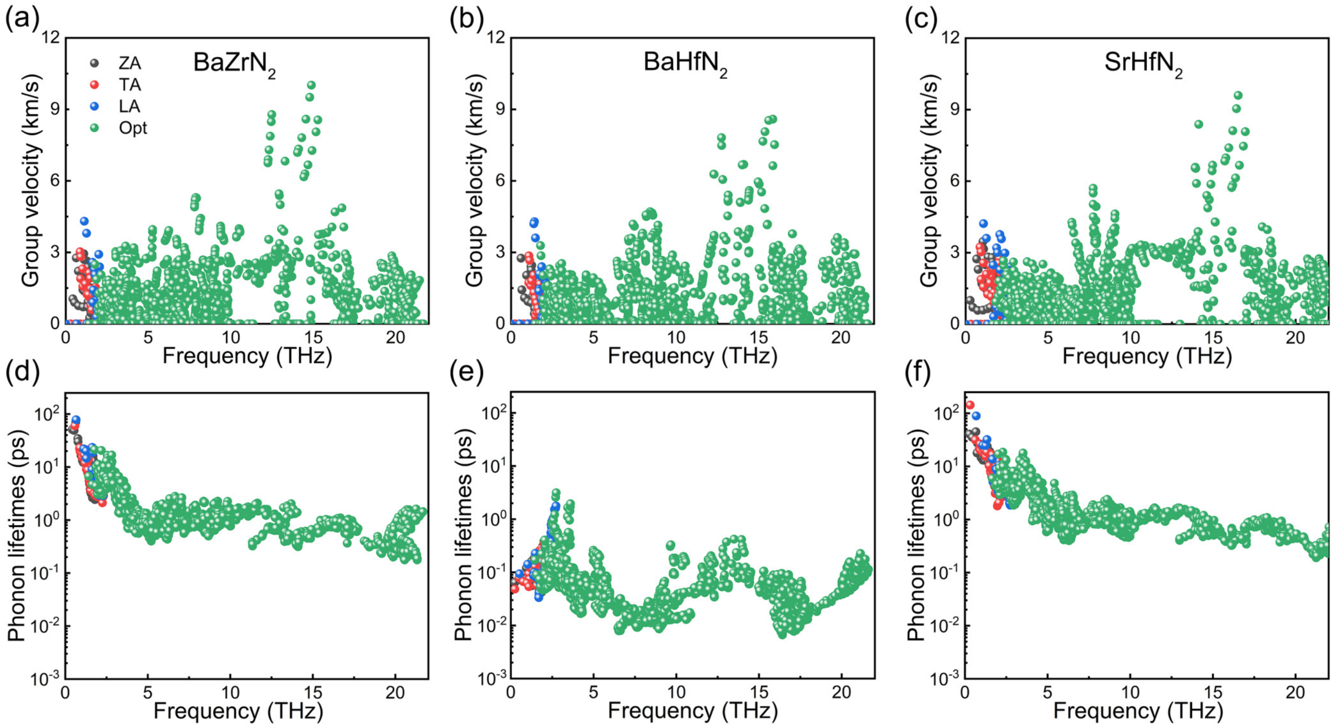

FIG. 5. (a)–(c) Phonon group velocities and (d)–(f) phonon lifetimes of BaZrN$_2$, BaHfN$_2$, and SrTiN$_2$. Black, red, blue, and green respectively represent *ZA*, TA, LA, and optical branch modes in the *AM*N$_2$ material at 300 K.

which is much lower than the lattice thermal conductivity of 0.18 W m^{-1} K^{-1}. In other words, the contribution of electronic thermal conductivity to the overall thermal conductivity is very small.

B. Electrical transport properties

To evaluate the electrical transport properties, we calculated the electron relaxation time as listed in Table I. For BaMN$_2$, the relaxation time is 1.74 fs for BaTiN$_2$, 9.72 fs for BaZrN$_2$, and 9.30 fs for BaHfN$_2$ at room temperature. The maximum relaxation time of SrHfN$_2$ is 25.98 fs. We then calculated the Seebeck coefficients (*S*) for both the *p*-type and *n*-type materials, as shown in Supplemental Material Fig. S6(c) and Figs. 6(a)–6(c). Clearly, *S* for *p*-type materials increases as temperature rises, while *S* for *n*-type materials follows the opposite trend. The calculated *S* at room temperature with carrier concentration of $1.0\times10^{20}/\mathrm{cm}^3$ are 250.24, 176.43, and 241.35 μV/K for *p*-type carriers and 81.00, 92.57, and 100.53 μV/K for *n*-type carriers in BaTiN$_2$, BaZrN$_2$, and BaHfN$_2$, respectively, which are comparable to that of commercial PbTe (∼100 μV/K for *n*-type carriers) [49]. A similar value of *S* is observed for the SrHfN$_2$. Subsequently, we explore the electrical conductivity (σ) as shown in Supplemental Material Fig. S6(d) and Figs. 6(d)–6(f). We find that the electrical conductivity for *p*-type BaZrN$_2$ (673.13 S/cm), BaHfN$_2$ (864.21 S/cm), and SrHfN$_2$ (1409.74 S/cm) is higher than that for *n*-type BaZrN$_2$ (311.08 S/cm), BaHfN$_2$ (401.29 S/cm), and SrHfN$_2$ (343.85 S/cm) except BaTiN$_2$. The exceptionally high electrical conductivity can be attributed to the unique two-dimensional conductive layers in *AM*N$_2$. It also is evident that the power factors of *p*-type and *n*-type *AM*N$_2$ exhibit anisotropy, as displayed in Figs. 6(h)–6(j). As the atomic mass of *M* increases, the power factor increases for both *p*-type and *n*-type materials. For instance, the power factor for *p*-type BaHfN$_2$ increased by about ten times compared to *p*-type BaTiN$_2$. In particular, room-temperature PF of *p*-type BaHfN$_2$ is 78.03 μW cm^{-1} K^{-2} which is much higher than that of *p*-type BaTiN$_2$ (8.01 μW cm^{-1} K^{-2}), BaZrN$_2$ (44.76 μW cm^{-1} K^{-2}), and SrHfN$_2$ (58.70 μW cm^{-1} K^{-2}). It is worthwhile to note that the room-temperature PFs of BaZrN$_2$, BaHfN$_2$, and SrHfN$_2$ are larger than that of SnSe (10.1 μW cm^{-1} K^{-2}) [10], indicating that the *AM*N$_2$ family has high performance of electrical transport.

C. Thermoelectric performance

Based on the calculated electrical and thermal transport properties, we evaluate the TE performance by calculating *ZT*, as shown in Figs. 6(k)–6(m). As expected, the maximum *ZT* of *p* type is significantly larger than that of *n* type due to the anisotropic power factor. At optimal carrier concentration, *p*-type BaHfN$_2$ exhibits an impressive *ZT* of 2.19 at room temperature. As the temperature increases, we find that *ZT* of both *p* type and *n* type further increases. Especially, *ZT* for *p*-type BaHfN$_2$ at 600 K and 900 K is as high as 5.13 and 7.29, respectively, which are much higher than the well-known *p*-type PbTe (1.5 at 773 K) [7]. Notably, *n*-type BaHfN$_2$ has a *ZT* of 1.85 at 900 K, suggesting that BaHfN$_2$ could be promising for practical TE devices. As a further step, we demonstrate that *ZT* of BaHfN$_2$ can be tuned through moderate strain engineering. For instance, introducing a tensile strain of 0.5% allows for the tuning of phonon dispersion, effectively suppressing lattice thermal conductivity. Conversely, applying a compressive strain of 0.5% to BaHfN$_2$ leads to an increase in lattice thermal conductivity (Fig. 7).

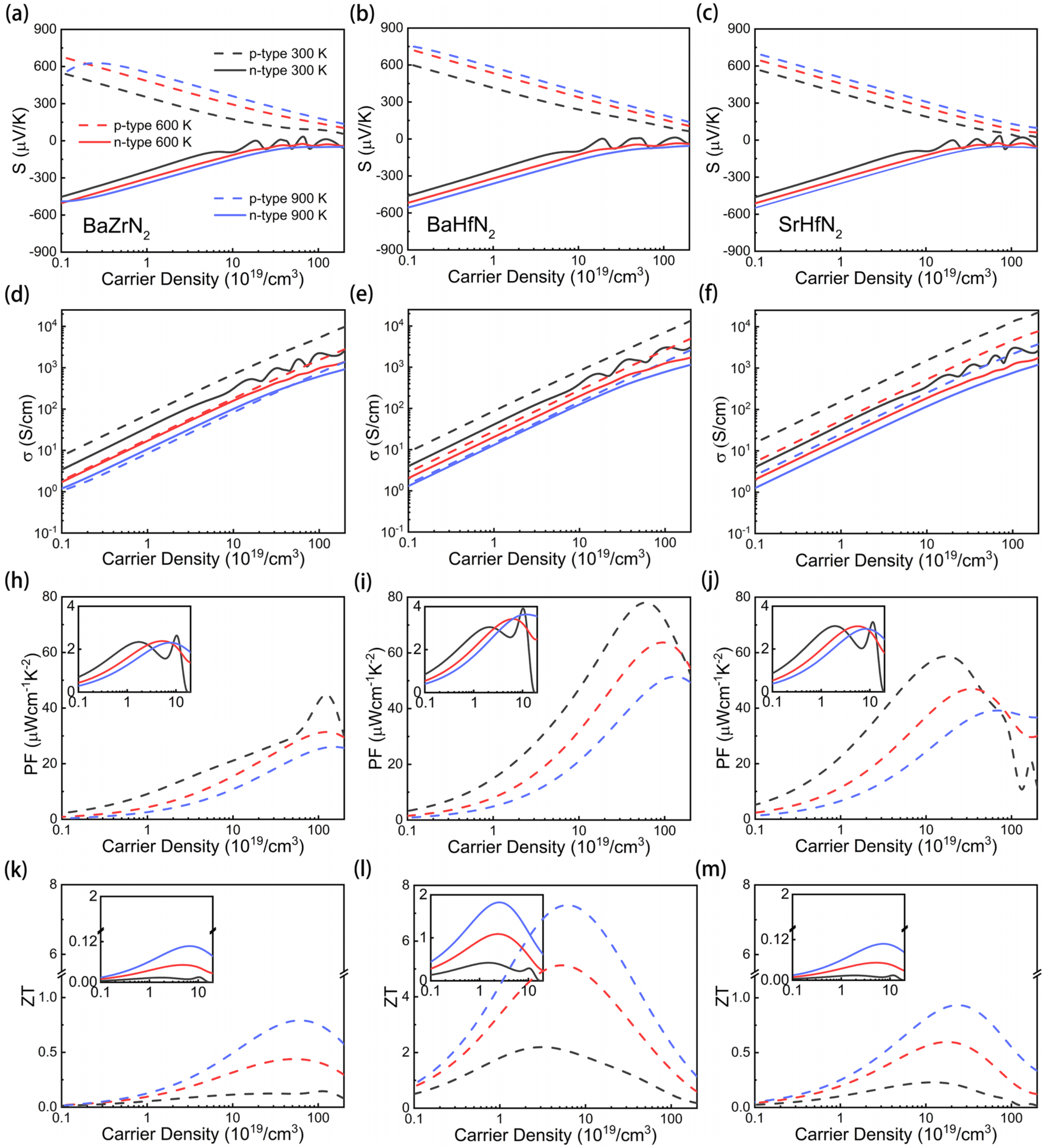

FIG. 6. Calculated Seebeck coefficient (a)–(c), electrical conductivity (d)–(f), and power factor (h)–(j) and figure of merit (k)–(m) as a function of carrier concentration and temperature for *p*-type (dashed line) and *n*-type (solid line) in $BaZrN_2$, $BaHfN_2$, and $SrHfN_2$. Note that power factor and figure of merit for *n*-type doping materials are displayed as inset. Black, red, and blue represent 300, 600, and 900 K, respectively.

It is found that introducing a strain has a negligible effect on the band structure and electrical transport of the material in Supplemental Material Figs. S8(a) and S8(b) and Figs. S6(b) and S6(c). Consequently, the room-temperature *ZT* of *p*-type $BaHfN_2$ reaches 2.58 under tensile strain of 0.5%, while it increases to 0.79 for *n* type, as shown in Fig. 7(f). At high temperature (900 K), *ZT* of *p*-type and *n*-type $BaHfN_2$ can be enhanced to as high as 9.02 and 3.00 under tensile strain of 0.5%, respectively, as displayed in Supplemental Material Fig. S9(d).

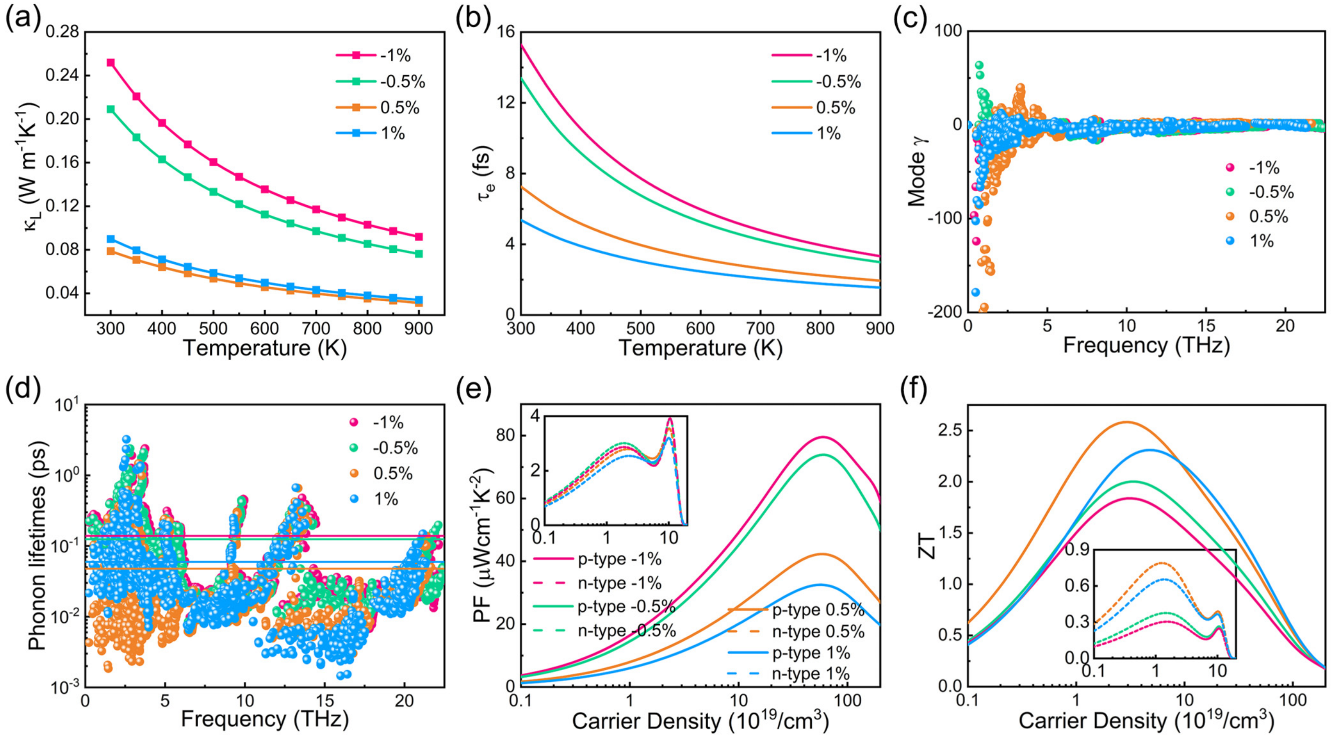

FIG. 7. (a) The temperature dependent lattice thermal conductivity κ_L and (b) relaxation time τ_e. (c), (d) The Grüneisen parameter and phonon lifetimes, respectively. (e), (f) The power factor and *ZT* vs strain in $BaHfN_2$ configurations at 300 K. Red and cyan indicate compression of 1% and 0.5%, and yellow and blue indicate stretching of 0.5% and 1%. The dashed line represents the *n* type and the solid line represents the *p* type.

V. WAVELIKE PHONON TRANSPORT

Recent studies have emphasized the importance of coherence contributions from nondiagonal terms of heat flux operators, i.e., a wavelike tunneling channel, in compounds with ultralow κ_L or/and strong anharmonicity [50]. We attempt to analyze the role of particlelike and wavelike conduction mechanisms in the AMN_2 family, and resolve the phonon lifetime (τ) as a function of phonon energy at room temperature by introducing the average phonon interband spacing to judge the strength of particlelike and wavelike conduction mechanisms, $\Delta\omega_{av} = \frac{\omega_{\max}}{3N_{at}}$, which is defined as the ratio between the maximum phonon frequency ($\omega_{\max}$) and the number of phonon bands ($3N_{at}$). Calculations have found that only $BaHfN_2$ has an average relaxation time (0.09) less than the Wigner time limit $\tau = \frac{1}{\Delta\omega_{av}}$ ($\sim$1), while other materials do not comply, indicating that $BaHfN_2$ exhibits both particlelike propagation and wavelike tunneling mechanisms in phonon modes.

In the framework of the Wigner formalism [51], the lattice thermal conductivity is generalized to an expression including the contributions of both populations and coherences: $\kappa_{\text{tot}} = \kappa_p + \kappa_c$. The first part is to obtain the lattice thermal conductivity of a particlelike conduction mechanism by iteratively solving the Boltzmann transport equation [52]. The second part is to calculate the lattice thermal conductivity of a wavelike conduction mechanism using the Wigner transport equation [53]. We calculated the thermal conductivity of $BaHfN_2$ as a function of temperature in Fig. 8(a).

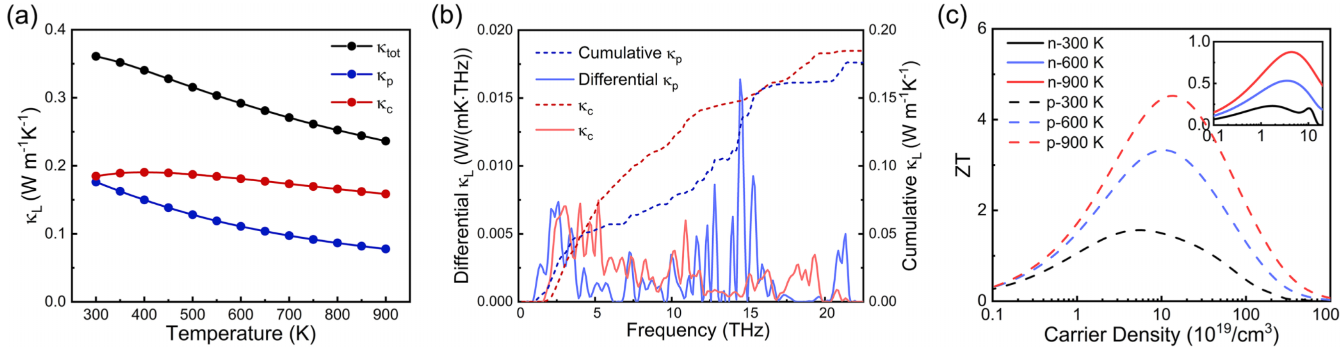

FIG. 8. (a) Temperature dependent thermal conductivity of $BaHfN_2$, where κ_p (blue) is the particlelike contribution and κ_c (red) is the wavelike contribution. (b) Phonon-mode-resolved and cumulative lattice thermal conductivity (κ_p and κ_c) as a function of phonon frequency at 300 K. (c) The thermoelectric figure of merit *ZT* as a function of carrier doping concentration of $BaHfN_2$ at 300, 600, and 900 K.

By considering the renormalization of force constants, the obtained κ_p and κ_c at 300 K are 0.176 and 0.184 W/mK, respectively, accounting for 49% and 51% of the total κ_L. In this case, the influence of the nondiagonal component of the heat flux operator cannot be ignored, and it can also overcome the shortcomings of the Peierls-Boltzmann heat transfer equation in ultralow or glasslike thermal conductivity crystals. With the increase of temperature, the significant scattering of κ_p shows a monotonic decreasing trend due to strong anharmonicity, while κ_c weakens the temperature dependence of thermal conductivity. At high temperature (900 K), the wavelike contribution to the total κ_L is as high as 67%, suggesting a strong wave tunneling mechanism for thermal transport in $BaHfN_2$. Figure 8(b) shows the contributions of κ_p and κ_c at 300 K under different phonon frequencies. κ_p mainly comes from low- and middle-frequency phonon modes, while almost all phonons contribute to κ_c throughout the entire frequency range. Based on the unified thermal transport theory, we calculated the carrier density dependent *ZT* of $BaHfN_2$ at different temperatures, as shown in Fig. 8(c). It is worth noting that even though considering the wavelike phonon transport, high *ZT* of *p*-type $BaHfN_2$ still remains, reaching 1.56 at 300 K and 4.52 at 900 K, respectively.

VI. CONCLUSIONS

In summary, we systematically investigate the electrical and thermal transport properties along with the thermoelectric performance of layered nitrides AMN_2 through first principles calculations combined with Boltzmann transport equation and thermal transport unified theory. The results show that the unique quasi-two-dimensional electronic properties in AMN_2 and highly anisotropic band structures remarkably enhance the electrical transport properties. Strong anharmonicity leads to the ultralow lattice thermal conductivity, as evidenced by the short phonon lifetime and large Grüneisen parameters. The combined high electrical transport and low lattice thermal conductivity gives rise to excellent thermoelectric performance in layered nitrides AMN_2. In addition, thermoelectric performance can be further improved through moderate strain engineering. The present work highlights the importance of unique two-dimensional electronic structures and strong anharmonicity on enhancing the overall thermoelectric performance in layered nitrides for potential application.

ACKNOWLEDGMENTS

This work was supported by National Natural Science Foundation of China (Grants No. 12174450 and No. 11874429), National Talents Program of China, The Science and Technology Innovation Program of Hunan Province (2024RC1013), Hundreds of Talents Program of Hunan Province, Key Project of Natural Science Foundation of Hunan Province (Grant No. 2024JJ3029), Hunan Provincial Key Research and Development Program (Grant No. 2022WK2002), Distinguished Youth Foundation of Hunan Province (Grant No. 2020JJ2039), Project of High-Level Talents Accumulation of Hunan Province (Grant No. 2018RS3021), State Key Laboratory of Powder Metallurgy, Start-up Funding and Innovation-Driven Plan of Central South University (Grant No. 2019CX023), and Postgraduate Scientific Research Innovation Project of Hunan Province (Grants No. CX20230104 and No. CX20220252). Calculations were performed at high-performance computing facilities of Central South University.

---

[1] X. Shi, L. Chen, and C. Uher, Recent advances in high-performance bulk thermoelectric materials, Int. Mater. Rev. **61**, 379 (2016).

[2] Q. Y. Yan and M. G. Kanatzidis, High-performance thermoelectrics and challenges for practical devices, Nat. Mater. **21**, 503 (2022).

[3] L. Y. Cheng, J. P. Yuan, M. L. Yao, M. Li, and H. Wang, Giant thermoelectric effect in rare earth sulfoiodides, J. Phys. Chem. C **127**, 20572 (2023).

[4] G. J. Tan, L. D. Zhao, and M. G. Kanatzidis, Rationally designing high-performance bulk thermoelectric materials, Chem. Rev. **116**, 12123 (2016).

[5] D. G. Xu, Q. Zhang, X. Y. Huo, Y. T. Wang, and M. L. Yang, Advances in data-assisted high-throughput computations for material design, MGE Adv. **1**, e11 (2023).

[6] L. D. Zhao, S. Q. Hao, S. H. Lo, C. I. Wu, X. Y. Zhou, Y. Lee, H. Li, K. Biswas, T. P. Hogan, C. Uher, C. Wolverton, V. P. Dravid, and M. G. Kanatzidis, High thermoelectric performance via hierarchical compositionally alloyed nanostructures, J. Am. Chem. Soc. **135**, 7364 (2013).

[7] J. P. Heremans, V. Jovovic, E. S. Toberer, A. Saramat, K. Kurosaki, A. Charoenphakdee, S. Yamanaka, and G. J. Snyder, Enhancement of thermoelectric efficiency in PbTe by distortion of the electronic density of states, Science **321**, 554 (2008).

[8] G. J. Snyder and E. S. Toberer, Complex thermoelectric materials, Nat. Mater. **7**, 105 (2008).

[9] J. P. Yuan, M. Li, and H. Wang, Intrinsically ultralow lattice thermal conductivity and giant thermoelectric effect in Ag-based intercalated layered crystalline solids, Phys. Rev. B **109**, 235202 (2024).

[10] L. D. Zhao, S. H. Lo, Y. S. Zhang, H. Sun, G. J. Tan, C. Uher, C. Wolverton, V. P. Dravid, and M. G. Kanatzidis, Ultralow thermal conductivity and high thermoelectric figure of merit in SnSe crystals, Nature (London) **508**, 373 (2014).

[11] X. L. Shi, J. Zou, and Z. G. Chen, Advanced thermoelectric design: From materials and structures to devices, Chem. Rev. **120**, 7399 (2020).

[12] L. Liu, M. J. Yao, Y. X. Wang, Y. Q. Jin, J. L. Ji, H. F. Luo, Y. Cao, Y. F. Xiong, Y. Sheng, X. Li, D. Qiu, L. L. Xi, J. Y. Xi, W. Q. Zhang, L. D. Chen, and J. Yang, The MatHub-3d first-principles repository and the applications on thermoelectrics, MGE Adv. **2**, e21 (2024).

[13] M. K. Brod, S. Anand, and G. J. Snyder, The importance of Mg-Sb interactions in achieving high conduction band degeneracy in Mg_3Sb_2 for high n-Type thermoelectric performance, Mater. Today Phys. **31**, 100959 (2023).

[14] Z. Guo, G. Wu, X. J. Tan, R. Y. Wang, Z. W. Zhang, G. J. Wu, Q. Zhang, J. H. Wu, G. Q. Liu, and J. Jiang, Enhanced

thermoelectric performance in GeTe by synergy of midgap state and band convergence, Adv. Funct. Mater. **33**, 2212421 (2023).

[15] Y. Z. Pei, X. Y. Shi, A. LaLonde, H. Wang, L. D. Chen, and G. J. Snyder, Convergence of electronic bands for high performance bulk thermoelectrics, Nature (London) **473**, 66 (2011).

[16] X. W. Zhang, C. H. Liu, Y. Tao, Y. H. Li, Y. L. Guo, Y. F. Chen, X. C. Zeng, and J. L. Wang, High ZT 2D thermoelectrics by design: Strong interlayer vibration and complete band-extrema alignment, Adv. Funct. Mater. **30**, 2001200 (2020).

[17] S. Mandal and P. Sarkar, Physical insights into the ultralow lattice thermal conductivity and high thermoelectric performance of bulk $\mathrm{LiMTe_2}$ ($M = $ Al, Ga), J. Mater. Chem. C **11**, 13691 (2023).

[18] T. T. Zhang, T. Yu, S. T. Ning, Z. Y. Zhang, N. Qi, M. Jiang, and Z. Q. Chen, Extremely low lattice thermal conductivity leading to superior thermoelectric performance in $\mathrm{Cu_4TiSe_4}$, ACS Appl. Mater. Interfaces **15**, 32453 (2023).

[19] L. Q. Xu, Y. Xiao, S. N. Wang, B. Cui, D. Wu, X. D. Ding, and L. D. Zhao, Dense dislocations enable high-performance PbSe thermoelectric at low-medium temperatures, Nat. Commun. **13**, 6449 (2022).

[20] A. I. Hochbaum, R. k. Chen, R. D. Delgado, W. J. Liang, E. C. Garnett, M. Najarian, A. Majumdar, and P. D. Yang, Enhanced thermoelectric performance of rough silicon nanowires, Nature (London) **451**, 163 (2008).

[21] J. Zhang, Y. Q. Xie, Y. B. Hu, and H. Z. Shao, Remarkable intrinsic ZT in the 2D $\mathrm{Pt}X_2$($X = $ O, S, Se, Te) monolayers at room temperature, Appl. Surf. Sci. **532**, 147387 (2020).

[22] I. Terasaki, Y. Sasago, and K. Uchinokura, Large thermoelectric power in $\mathrm{NaCo_2O_4}$ single crystals, Phys. Rev. B **56**, R12685(R) (1997).

[23] I. Ohkubo and T. Mori, Two-dimensional layered complex nitrides as a new class of thermoelectric materials, Chem. Mater. **26**, 2532 (2014).

[24] X. Y. He, Z. W. Xiao, T. Katase, K. Ide, H. Hosono, and T. Kamiya, Intrinsic and extrinsic defects in layered nitride semiconductor $\mathrm{SrTiN_2}$, J. Phys. Chem. C **123**, 19307 (2019).

[25] I. Ohkubo and T. Mori, Origin of projected excellent thermoelectric transport properties in $\mathrm{d^0}$-electron $AM\mathrm{N_2}$ ($A = $ Sr or Ba; $M = $ Ti, Zr, Hf) layered complex metal nitrides, Eur. J. Inorg. Chem. **2015**, 3715 (2015).

[26] C. Cancellieri, M. L. Reinle-Schmitt, M. Kobayashi, V. N. Strocov, P. R. Willmott, D. Fontaine, P. Ghosez, A. Filippetti, P. Delugas, and V. Fiorentini, Doping-dependent band structure of $\mathrm{LaAlO_3/SrTiO_3}$ interfaces by soft x-ray polarization-controlled resonant angle-resolved photoemission, Phys. Rev. B **89**, 121412(R) (2014).

[27] M. Salluzzo, J. C. Cezar, N. B. Brookes, V. Bisogni, G. M. De Luca, C. Richter, S. Thiel, J. Mannhart, M. Huijben, A. Brinkman, G. Rijnders, and G. Ghiringhelli, Orbital reconstruction and the two-dimensional electron gas at the $\mathrm{LaAlO_3/SrTiO_3}$ interface, Phys. Rev. Lett. **102**, 166804 (2009).

[28] L. D. Zhao, D. Berardan, Y. L. Pei, C. Byl, L. Pinsard-Gaudart, and N. Dragoe, $\mathrm{Bi}_{1-x}\mathrm{Sr}_x\mathrm{CuSeO}$ oxyselenides as promising thermoelectric materials, Appl. Phys. Lett. **97**, 092118 (2010).

[29] R. A. R. A. Orabi, E. Orisakwe, D. Wee, B. Fontaine, R. Gautier, J. F. Halet, and M. Fornari, Prediction of high thermoelectric potential in $AM\mathrm{N_2}$ layered nitrides: Electronic structure, phonons, and anharmonic effects, J. Mater. Chem. A **3**, 9945 (2015).

[30] S. Wang, J. S. Wang, C. P. Xue, X. H. Yang, G. Y. Tian, H. Su, Y. S. Miao, Q. Li, and X. X. Li, Unexpected nucleation mechanism of $\mathrm{T_1}$ precipitates by Eshelby inclusion with unstable stacking faults, MGE Adv. **2**, e33 (2024).

[31] M. L. Yao, X. Xu, M. Li, and H. Wang, Possible origin of low-frequency magnetic flux noise in superconducting devices, J. Phys. Chem. Lett. **14**, 1854 (2023).

[32] G. Kresse and J. Furthmüller, Efficient iterative schemes for ab initio total-energy calculations using a plane-wave basis set, Phys. Rev. B **54**, 11169 (1996).

[33] Z. C. Yang, M. L. Yao, J. Pan, L. K. Huang, M. Li, and H. Wang, Large magnetostriction of heavy-metal-element doped Fe-based alloys, J. Appl. Phys. **132**, 215105 (2022).

[34] M. L. Yao, J. Pan, W. F. Xie, Z. C. Yang, M. Li, and H. Wang, Control of the magnetic anisotropy and Curie temperature of monolayer 1T-$\mathrm{CrTe_2}$ for room temperature application, Appl. Phys. Lett. **123**, 242405 (2023).

[35] G. Kresse and J. Hafner, *Ab initio* molecular dynamics for liquid metals, Phys. Rev. B **47**, 558 (1993).

[36] F. Ren, M. L. Yao, M. Li, and H. Wang, Tailoring the structural and electronic properties of graphene through ion implantation, Materials **14**, 5080 (2021).

[37] A. Togo, F. Oba, and I. Tanaka, First-principles calculations of the ferroelastic transition between rutile-type and $\mathrm{CaCl_2}$-type $\mathrm{SiO_2}$ at high pressures, Phys. Rev. B **78**, 134106 (2008).

[38] W. Li, J. Carrete, A. K. Nebil, and N. Mingo, ShengBTE: A solver of the Boltzmann transport equation for phonons, Comput. Phys. Commun. **185**, 1747 (2014).

[39] W. F. Xie, X. Xu, F. B. Li, G. W. Zhai, Y. L. Yue, M. Li, and H. Wang, Large magnetocaloric refrigeration performance near room temperature in monolayer transition metal dihalides, Appl. Phys. Lett. **125**, 033903 (2024).

[40] See Supplemental Material at http://link.aps.org/supplemental/10.1103/PhysRevB.110.115202 for convergence testing, calculation details of enthalpy formation, thermal stability analysis, two-dimensional Brillouin zone diagram, some explanation of anharmony, thermoelectric properties of $\mathrm{BaTiN_2}$ material, conductivity under *p*-type doping, electrical and thermal transport properties of $\mathrm{BaHfN_2}$ under stress.

[41] P. Giannozzi, S. Baroni, N. Bonini, M. Calandra, R. Car, C. Cavazzoni, D. Ceresoli, G. L. Chiarotti, M. Cococcioni, I. Dabo, A. Dal Corso, S. de Gironcoli, S. Fabris, G. Fratesi, R. Gebauer, U. Gerstmann, C. Gougoussis, M. Lazzeri, A. Kokalj, L. Martin-Samos *et al.*, Quantum Espresso: A modular and open-source software project for quantum simulations of materials, J. Phys.: Condens. Matter **21**, 395502 (2009).

[42] G. K. H. Madsen and D. J. Singh, BoltzTraP. A code for calculating band-structure dependent quantities, Comput. Phys. Commun. **175**, 67 (2006).

[43] E. Orisakwe, B. Fontaine, D. H. Gregory, R. Gautier, and J. F. Halet, Theoretical study on the structural, electronic and physical properties of layered alkaline-earth-group-4 transition-metal nitrides $\mathrm{AEMN_2}$, RSC Adv. **4**, 31981 (2014).

[44] A. Shiraishi, S. Kimura, X. Y. He, N. Watanabe, T. Katase, K. Ide, M. Minohara, K. Matsuzaki, H. Hiramatsu, H. Kumigashira, H. Hosono, and T. Kamiya, Design, synthesis, and optoelectronic properties of the high-purity phase in layered $\mathrm{AETMN_2}$ (AE = Sr, Ba; TM = Ti, Zr, Hf) semiconductors, Inorg. Chem. **61**, 6650 (2022).

[45] Z. H. Yang, J. S. Wang, C. Zhang, S. Wang, C. P. Xue, G. Y. Tian, H. Su, C. M. Yan, Z. F. Yan, and Y. C. Tian, First-principle screening of corrosion resistant solutes (Al, Zn, Y, Ce, and Mn) in Mg alloys for integrated computational materials engineering guided stainless Mg design, MGE Adv. **2**, e22 (2024).

[46] D. H. Gregory, M. G. Barker, P. P. Edwards, M. Slaski, and D. J. Siddons, Synthesis, structure, and magnetic properties of the new ternary nitride $\mathrm{BaHfN_2}$ and of the $\mathrm{BaHf_{1-x}Zr_xN_2}$ solid solution, J. Solid State Chem. **137**, 62 (1998).

[47] O. Seeger, M. Hofmann, J. Strähle, J. P. Laval, and B. Frit, Synthesis and structure of $\mathrm{Ba[ZrN_2]}$ and $\mathrm{Ba_2[NbN_3]}$, Z. Anorg. Allg. Chem. **620**, 2008 (1994).

[48] X. Xu, F. B. Li, C. Niu, M. Li, and H. Wang, Machine learning assisted investigation of the barocaloric performance in ammonium iodide, Appl. Phys. Lett. **122**, 043901 (2023).

[49] L. W. Fu, M. J. Yin, Di. Wu, W. Li, D. Feng, L. Huang, and J. Q. He, Large enhancement of thermoelectric properties in n-type PbTe via dual-site point defects, Energy Environ. Sci. **10**, 2030 (2017).

[50] M. Simoncelli, N. Marzari, and F. Mauri, Unified theory of thermal transport in crystals and glasses, Nat. Phys. **15**, 809 (2019).

[51] J. E. Moyal, Quantum mechanics as a statistical theory, Math. Proc. Cambridge **45**, 99 (1949).

[52] A. J. H. McGaughey, A. Jain, H. Y. Kim, and B. Fu, Phonon properties and thermal conductivity from first principles, lattice dynamics, and the Boltzmann transport equation, J. Appl. Phys. **125**, 011101 (2019).

[53] M. Simoncelli, N. Marzari, and F. Mauri, Wigner formulation of thermal transport in solids, Phys. Rev. X **12**, 041011 (2022).